

Mid-infrared colors as a diagnostic tool of circumstellar envelopes in AGB stars[★]

M. Marengo^{1,2}, M. Busso³, G. Silvestro⁴, P. Persi⁵, and P.O. Lagage⁶

¹ SISSA – Int. School for Advanced Studies, Trieste, Italy

² Harvard-Smithsonian Center for Astrophysics, Cambridge, Massachusetts, USA

³ Osservatorio Astronomico di Torino, Pino Torinese, Italy

⁴ Dipartimento di Fisica Generale, Università di Torino, Italy

⁵ Istituto di Astrofisica Spaziale CNR, Roma, Italy

⁶ DSM/DAPNIA/Service d'Astrophysique – CEA Saclay, Gif-sur-Yvette, France

Received 8 April 1999 / Accepted 16 June 1999

Abstract. New observations of AGB circumstellar envelopes made with the mid-IR imaging camera CAMIRAS are presented. Diagnostic tools based on mid-IR colors are proposed for the analysis of the observed objects, and tested against a larger sample of AGB sources derived from IRAS observations. Radiative transfer modelling is used to calibrate our diagnostic procedures, in order to investigate the physical and chemical characteristics of both samples. The different chemical signatures of C-rich and O-rich envelopes are put in evidence by mid-IR color-color diagrams, and correlations are found between the observed colors and a mass loss parameter derived by radio observations. Evidences for possible temporal variations in the mass loss rates are also suggested. The possibility to derive direct information on the spatial structure and symmetry of the envelopes is finally investigated, and the image of the O-rich star WX Psc, as an example of a spatially resolved axisymmetric envelope, is presented.

Key words: stars: AGB and post-AGB – stars: circumstellar matter – stars: individual: 0191-B2B – infrared: stars

1. Introduction

Low mass stars (LMS) and intermediate mass stars (IMS), in the late evolutionary stages populate a sequence in the H-R diagram known as the Asymptotic Giant Branch (AGB). Here they undergo intense mass loss, responsible for the creation of a circumstellar envelope of gas and dust. This envelope is often opaque to visible photons coming from the central star, due to dust grains condensing in the stellar extended atmosphere. It is nonetheless a source of thermal infrared (IR) radiation, especially in the range 5–20 μm . For this reason, and for the optical properties of silicates, amorphous carbon and silicon carbide (SiC), that are the main constituents of circumstellar grains, mid-IR wave-

lengths are a preferred diagnostic tool to investigate the physical and chemical composition of dusty circumstellar environments around AGB stars (Waters et al. 1998; Blommaert et al. 1998; Zijlstra et al. 1996; Willems & de Jong 1988; van der Veen & Habing 1988). The composition and properties of AGB circumstellar environments derive from the chemical mix in the stellar convective envelope, and in particular from the C/O abundance ratio. This is in turn determined by the initial mass M_i of the star, and by the time spent on the AGB, that set strong limits on the creation of a *carbon star* (having C/O ≥ 1 in the photosphere) from an O-rich M-giant entering the AGB phase. The C enrichment of the convective envelope is the consequence of a mixing process known as *third dredge-up*. It occurs repeatedly on the AGB, after thermal instabilities of the He-shell that interrupt the normal power release by the H-burning shell (Iben & Renzini 1983; Busso et al. 1999).

Recently, updated stellar models (Straniero et al. 1995, 1997) found that, for solar metallicity, only stars above 1.5–2.0 M_\odot can undergo a sufficient number of third dredge-up episodes to drive an increase of the C/O ratio above unity. On the other hand, AGB stars with $M_i \gtrsim 5\text{--}6 M_\odot$ experience partial H-burning at the base of the convective envelope (Hot Bottom Burning, or HBB, see e.g. Sugimoto 1971; Renzini & Voli 1981; Blöcker & Schönberner 1991; Sackmann & Boothroyd 1992; Vassiliadis & Wood 1993; Frost et al. 1998). This consumes the newly produced C, preventing the stars from becoming C-rich (however, see Frost et al. 1998). As a result, C stars can probably be formed at the end of AGB evolution in a quite narrow mass range (2–4 M_\odot). More massive AGB stars appear to be Li-rich, and are of class S (Smith & Lambert 1989); in general, O-rich envelopes are therefore expected around very different objects, either of very low mass ($M \lesssim 2 M_\odot$) or rather massive ($M \gtrsim 5 M_\odot$), and in very different evolutionary stages. This is directly reflected in the larger variety of O-rich envelopes, compared to the rather uniform properties of the C-rich ones.

In this paper, we want to show that this dichotomy is reflected in the mid-IR properties of the two classes of sources and to derive criteria for discriminating them and/or understanding

Send offprint requests to: M. Marengo

[★] Based on observations made at the Italian Infrared Telescope of Gornergrat (TIRGO)

Table 1. Mid-IR flux densities of the observed (CAMIRAS) AGB stars.

| Source | $F_{8.55}$ [Jy] | $F_{8.57}$ [Jy] | $F_{9.56}$ [Jy] | $F_{11.21}$ [Jy] | $F_{12.24}$ [Jy] | $F_{12.45}$ [Jy] | $F_{16.64}$ [Jy] | epoch |
|-----------------|--------------------|--------------------|--------------------|---------------------|---------------------|---------------------|---------------------|---------|
| KU And | 488 | 433 | 763 | 1030 | – | 497 | – | Nov. 96 |
| WX Psc | 846 | 702 | 1050 | 1040 | – | 364 | 863 | Nov. 96 |
| W And | 154 | 151 | 188 | 162 | – | 115 | – | Nov. 96 |
| CRL 618 | 226 | 192 | 322 | 378 | 413 | 484 | 882 | Nov. 96 |
| | – | – | 272 | – | 559 | – | – | Feb. 97 |
| IRAS 06088+1909 | 40 | – | 37 | 42 | – | 37 | – | Nov. 96 |
| Red Rectangle | 235 | – | 937 | – | – | – | 3030 | Feb. 97 |
| IRC+40156 | – | 54 | – | 76 | 50 | – | – | Nov. 96 |
| CIT 6 | – | – | – | 3880 | 3070 | – | 1930 | Feb. 97 |
| NSV 9118 | 221 | – | 283 | 222 | 290 | – | – | Feb. 97 |
| CRL 3068 | 288 | – | 362 | 404 | – | 472 | 280 | Nov. 96 |

their properties from their infrared emission. For a more general discussion of AGB evolution and nucleosynthesis the reader is referred to Busso et al. (1999). The various classes of carbon stars are discussed at length in the review by Wallerstein and Knapp (1998).

This work extends a previous analysis of a sample of AGB circumstellar envelopes performed with the 10–20 μm imaging camera TIRCAM, aimed at analyzing the correlation between mass loss rates and mid-IR colors in the AGB phase (Busso et al. 1996, hereafter paper I), and the subsequent modelling needed to derive the physical parameters of the observed objects (Marengo et al. 1997, hereafter paper II). New observations with the IR camera CAMIRAS (Lagage et al. 1992) have been carried out to measure IR colors of a larger sample of C-rich and O-rich sources, and to explore the possibility of direct imaging of the AGB circumstellar envelopes. The details of the observational runs are presented in Sect. 2; the sample characteristics are given in Sect. 3, while in Sect. 4 mid-IR colors are derived and the relationship between colors and mass loss is discussed.

In Sect. 5 we compare the results for our sources with simulations computed using a much larger sample compiled by Loup et al. (1993), hereafter L93, for which mid-IR colors are derived from a rebinning of the IRAS Low Resolution Spectra (1986). Simple radiative transfer modelling (Ivezić & Elitzur 1997) is then used for the interpretation of both samples, and to investigate the physics of mass loss in the AGB phase from mid-IR data.

Near infrared observations of AGB and post-AGB objects from space (Sahai et al. 1998) and from the ground (Weigelt et al. 1998; Monnier et al. 1998) reveal how mass loss in the AGB phases is variable on different timescales, and modulated by various periodicities, such as the thermal pulses (Steffen et al. 1998), LPV-Mira pulsations (Le Bertre & Winters 1998) and dynamical times for dust condensation (Fleischer et al. 1992; Winters et al. 1994, 1995). Imaging in the mid-IR is complementary to high resolution observations in the near-IR (that can only access the hotter regions where dust is condensing near the stellar photosphere) or to radio interferometric data (mapping the spatial distributions of molecular gas at much larger distances from the star). The required sub-arcsec angular resolution can

be achieved using medium and large aperture telescopes on the ground, and with very short integration times to obtain nearly diffraction limited images. To demonstrate the feasibility of this technique, we present in Sect. 6 the mid-IR images of an AGB source (WX Psc), for which we were able to spatially resolve the extended emission from circumstellar dust, revealing departures from spherical symmetry and a complex mass loss history over the timescale in which the envelope was formed.

The main results of our work are then summarized and discussed in Sect. 7.

2. Observations

Mid-IR images of ten AGB stars were obtained in November 1996 and February 1997 using the mid-IR camera CAMIRAS developed at the Service d’Astrophysique at Saclay (Lagage et al. 1992) equipped with a 192×128 Si:Ga/DVR array detector, and mounted at the 1.5m Italian Infrared telescope of Gornergrat (TIRGO). We used a scale of $0.72''/\text{pix}$ and a set of 10% pass-band filters centered at 8.55, 9.56, 11.21, 12.45 and $16.64 \mu\text{m}$, plus narrow band filters at 8.57 and $12.24 \mu\text{m}$. The sky and telescope emissions were subtracted using the standard chopping and nodding techniques for observations in high background conditions. In order to have a good image quality, each observation was split in many short exposures (2–10 seconds), then recentered and coadded to obtain the required total integration time (from 5 to 15 minutes, according to the source brightness). The secondary mirror throw (for chopping) and the nodding angle were chosen in order to have the target in all four beams, thus maximizing the signal of the sources and minimizing the total integration time.

The standard stars α Ari, α Aur, α Tau, β And, β Gem, and β Peg were observed to calibrate the images and to derive the point-spread-function (PSF). The calibration fluxes in the CAMIRAS photometric system were derived for each standard in a two step process: (1) a synthetic spectrum for each star was constructed by fitting available IR photometric data (Gezari 1993) with a modified black body (Engelke 1992), and then (2) convolved with CAMIRAS filter profiles to provide the flux at each wavelength. The observed PSF varies from night to night, and in the mean is $\sim 2.2''$ at $8.55 \mu\text{m}$ and $\sim 3''$ at $12.45 \mu\text{m}$.

Table 2. List of the observed sources (TIRCAM+CAMIRAS). For each source the IRAS name and IRAS LRS code are indicated. The chemical class of the envelope, the variability type, the bolometric flux (in units of the source luminosity for a “standard” distance of 1 kpc), the mass loss estimate, the gas outflow velocity and the distance are obtained from L93. The total luminosity is computed as $L = 4\pi \cdot 1\text{kpc}^2 \cdot F_{total}/d^2$, and is thus affected by the errors in the distance determination and bolometric flux estimate by L93 (based on IRAS colors, and thus quite crude for objects whose spectra are dominated by near-IR emission). Note that, in some cases, more than one estimate exists for the mass loss rate, and/or distance and luminosity.

| # | Source | Class | IRAS | LRS | Var.type | $4\pi \cdot 1\text{kpc}^2 F_{total}$ L_{\odot} | \dot{M} [$M_{\odot} \text{ yr}^{-1}$] | v_e [km s^{-1}] | d [kpc] | L [L_{\odot}] |
|----|-----------------|--------|------------|-----|----------|---|---|---------------------------------|--------------------------------------|--|
| 1 | KU And | O-rich | 00042+4248 | 26 | M | $1.5 \cdot 10^4$ | $9.7 \cdot 10^{-6}$ $2.4 \cdot 10^{-5}$ | 21.7 21.7 | 0.82 1.10 | $1.0 \cdot 10^4$ $1.8 \cdot 10^4$ |
| 2 | WX Psc | O-rich | 01037+1219 | 4n | M | $3.4 \cdot 10^4$ | $8.5 \cdot 10^{-6}$ $1.2 \cdot 10^{-5}$ $2.4 \cdot 10^{-5}$ | 20.7 20.7 20.7 | 0.54 0.51 0.51 | $9.9 \cdot 10^3$ $8.8 \cdot 10^3$ $8.8 \cdot 10^3$ |
| 3 | W And | S-star | 02143+4404 | 22 | M | $4.4 \cdot 10^4$ | $8.0 \cdot 10^{-7}$ $9.7 \cdot 10^{-7}$ | 10.7 10.7 | 0.48 0.63 | $1.0 \cdot 10^3$ $1.7 \cdot 10^3$ |
| 4 | o Cet | O-rich | 02168-0312 | 2n | M | $8.1 \cdot 10^5$ | $5.0 \cdot 10^{-7}$ $5.7 \cdot 10^{-7}$ $1.0 \cdot 10^{-6}$ $1.0 \cdot 10^{-7}$ $2.1 \cdot 10^{-6}$ | 5.6 5.6 5.6 5.6 5.6 | 0.11 0.08 0.08 0.08 0.08 | $9.8 \cdot 10^3$ $5.1 \cdot 10^3$ $5.1 \cdot 10^3$ $5.1 \cdot 10^3$ $5.1 \cdot 10^3$ |
| 5 | CRL 618 | C-rich | 04395+3601 | 62 | – | $7.8 \cdot 10^3$ | $6.7 \cdot 10^{-5}$ $5.6 \cdot 10^{-5}$ | 19.5 19.5 | 1.30 1.30 | $1.3 \cdot 10^4$ $1.7 \cdot 10^4$ |
| 6 | IRAS 06088+1909 | C-rich | 06088+1909 | – | – | – | – | – | – | – |
| 7 | Red Rect | C-rich | 06176-1036 | 80 | – | – | – | – | – | – |
| 8 | IRC+40156 | O-rich | 06297+4045 | 27 | – | $3.7 \cdot 10^3$ | $1.0 \cdot 10^{-5}$ | 16.3 | 1.60 | $9.5 \cdot 10^3$ |
| 9 | X CnC | C-rich | 08525+1725 | 42 | SRb | $2.1 \cdot 10^4$ | $7.7 \cdot 10^{-7}$ $4.6 \cdot 10^{-7}$ | 9.7 9.7 | 0.69 0.64 | $1.0 \cdot 10^4$ $8.6 \cdot 10^3$ |
| 10 | R LMi | O-rich | 09425+3444 | 24 | M | $9.4 \cdot 10^4$ | $2.8 \cdot 10^{-7}$ $5.0 \cdot 10^{-7}$ | 7.0 7.0 | 0.33 0.35 | $1.0 \cdot 10^4$ $1.2 \cdot 10^4$ |
| 11 | R Leo | O-rich | 09448+1139 | 1n | M | $5.0 \cdot 10^5$ | $1.0 \cdot 10^{-7}$ $8.0 \cdot 10^{-8}$ $6.0 \cdot 10^{-7}$ | 8.5 8.5 8.5 | 0.14 0.30 0.24 | $9.8 \cdot 10^3$ $4.5 \cdot 10^4$ $2.9 \cdot 10^4$ |
| 12 | CW Leo | C-rich | 09452+1330 | 43 | M | $6.6 \cdot 10^5$ | $4.8 \cdot 10^{-5}$ $2.2 \cdot 10^{-5}$ | 14.7 14.7 | 0.29 0.22 | $5.6 \cdot 10^4$ $5.6 \cdot 10^4$ |
| 13 | CIT 6 | C-rich | 10131+3049 | 04 | SRa | $6.9 \cdot 10^4$ | $6.0 \cdot 10^{-6}$ $2.6 \cdot 10^{-6}$ $4.8 \cdot 10^{-6}$ $7.5 \cdot 10^{-6}$ | 16.8 16.8 16.8 16.8 | 0.38 0.19 0.39 0.48 | $1.0 \cdot 10^4$ $2.5 \cdot 10^3$ $1.0 \cdot 10^4$ $1.6 \cdot 10^4$ |
| 14 | Y CVn | C-rich | 12427+4542 | 42 | SRb | $8.7 \cdot 10^4$ | $4.2 \cdot 10^{-7}$ $2.8 \cdot 10^{-7}$ $1.4 \cdot 10^{-6}$ $1.2 \cdot 10^{-7}$ | 8.2 8.2 8.2 8.2 | 0.34 0.35 0.35 0.41 | $1.0 \cdot 10^4$ $1.1 \cdot 10^4$ $1.1 \cdot 10^4$ $1.5 \cdot 10^4$ |
| 15 | RT Vir | O-rich | 13001+0527 | 21 | SRb | $1.3 \cdot 10^5$ | $7.4 \cdot 10^{-7}$ $1.3 \cdot 10^{-6}$ $6.0 \cdot 10^{-6}$ $4.9 \cdot 10^{-7}$ | 9.3 9.3 9.3 9.3 | 0.28 0.97 1.00 0.32 | $1.0 \cdot 10^4$ $1.2 \cdot 10^5$ $1.3 \cdot 10^5$ $1.3 \cdot 10^4$ |
| 16 | S CrB | O-rich | 15193+3132 | 24 | M | $2.3 \cdot 10^4$ | $5.8 \cdot 10^{-7}$ $6.0 \cdot 10^{-7}$ | 6.3 6.3 | 0.66 0.42 | $1.0 \cdot 10^4$ $4.1 \cdot 10^3$ |
| 17 | WX Ser | O-rich | 15255+1944 | 29 | M | $7.2 \cdot 10^3$ | $2.6 \cdot 10^{-6}$ $5.3 \cdot 10^{-7}$ | 8.8 8.8 | 1.20 0.72 | $1.0 \cdot 10^3$ $3.7 \cdot 10^3$ |
| 18 | V CrB | C-rich | 15477+3943 | 4n | M | $1.5 \cdot 10^4$ | $5.2 \cdot 10^{-7}$ $5.8 \cdot 10^{-7}$ | 7.8 7.8 | 0.82 1.02 | $1.0 \cdot 10^4$ $1.6 \cdot 10^4$ |
| 19 | U Her | O-rich | 16235+1900 | 23 | M | $3.2 \cdot 10^5$ | $2.6 \cdot 10^{-7}$ | 13.1 | 0.18 | $1.0 \cdot 10^4$ |
| 20 | NSV 9118 | O-rich | 17297+1747 | 14 | SR | $1.6 \cdot 10^4$ | $9.7 \cdot 10^{-6}$ $2.0 \cdot 10^{-5}$ $1.6 \cdot 10^{-5}$ | 16.3 16.3 16.3 | 0.79 1.20 1.20 | $1.0 \cdot 10^4$ $2.3 \cdot 10^4$ $2.3 \cdot 10^4$ |
| 21 | RAFGL 2205 | O-rich | 18348-0526 | 3n | M | $1.1 \cdot 10^4$ | $2.1 \cdot 10^{-6}$ | 10.6 | 0.95 | $9.9 \cdot 10^4$ |

Table 2. (continued)

| # | Source | Class | IRAS | LRS | Var.type | $4\pi \cdot 1\text{kpc}^2 F_{total}$ L_{\odot} | \dot{M} [$M_{\odot} \text{ yr}^{-1}$] | v_e [km s^{-1}] | d [kpc] | L [L_{\odot}] |
|----|-----------|--------|------------|-----|----------|---|--|---------------------------------|------------|------------------------|
| 22 | NSV 11225 | C-rich | 18397+1738 | 43 | – | $2.8 \cdot 10^4$ | $3.8 \cdot 10^{-6}$ | 14.2 | 0.60 | $1.0 \cdot 10^4$ |
| | | | | | | | $9.1 \cdot 10^{-6}$ | 14.2 | 0.79 | $1.7 \cdot 10^4$ |
| | | | | | | | $2.4 \cdot 10^{-6}$ | 14.2 | 0.79 | $1.7 \cdot 10^4$ |
| | | | | | | | $6.0 \cdot 10^{-6}$ | 14.2 | 0.64 | $1.1 \cdot 10^4$ |
| 23 | CRL 3068 | C-rich | 23166+1655 | 02 | – | $1.1 \cdot 10^4$ | $8.4 \cdot 10^{-6}$ | 14.1 | 0.95 | $9.9 \cdot 10^3$ |
| | | | | | | | $6.4 \cdot 10^{-6}$ | 14.1 | 0.57 | $3.6 \cdot 10^3$ |
| | | | | | | | $1.2 \cdot 10^{-5}$ | 14.1 | 1.00 | $1.1 \cdot 10^4$ |
| | | | | | | | $2.1 \cdot 10^{-5}$ | 14.1 | 1.04 | $1.2 \cdot 10^4$ |

In Table 1 we report the integrated flux densities of our observed AGB stars. The photometric statistical error (comprehensive of the calibration errors) is approximately 10%. Of all the observed AGB stars in Table 1, only WX Psc and the Red Rectangle appear to be spatially resolved (within our measured PSF) in all the filters, while most of the other sources are unresolved, or show extended mid-IR emissions only in the shortest wavelength filters (where the PSF is smaller).

3. The AGB sample

In order to increase the statistical significance of our data on mid-IR fluxes for AGB stars, we have enlarged our sample, adding the mid-IR data of other AGBs previously taken with the camera TIRCAM (paper I). Since TIRCAM observations were carried out using a slightly different photometric system (8.8, 9.8, 11.2 and $12.5 \mu\text{m}$), the IRAS LRS of some AGB sources of different chemical type in our sample were used to estimate the color corrections needed to compare data in the $8.55 \mu\text{m}$ filter with those in the $8.8 \mu\text{m}$ one, and data in the $9.56 \mu\text{m}$ filter with those in the $9.8 \mu\text{m}$ one. These color corrections, however, turned out to be much smaller than the uncertainty of the measurements in our photometry, and have therefore been ignored in the present work.

All the data presented in paper I were revised during the preparation of this paper, in order to ensure an homogeneous quality of the photometry in the combined sample. For this reason the C-rich TIRCAM source FX Ser was rejected, due to a vignetting of the original image in the $8.8 \mu\text{m}$ filter. The TIRCAM photometry of the S-star W And reported in paper I was also discarded in favour of the more accurate CAMIRAS photometry of the same source, since the $12.5 \mu\text{m}$ TIRCAM image of W And was found to be contaminated by a residual background signal.

The complete list of AGB stars considered here is reported in Table 2. Each source is chemically characterized by its IRAS LRS code (based on the features of the IRAS 7–23 μm Low Resolution Spectra), and by the “chemical type” of the envelope, as given in L93. For all the variable sources, the variability type is also reported (again from L93).

One or more estimates of the mass loss rate, derived from CO/HCN radio millimetric observations, are available in L93 for many of the sources in our list. Table 2 reports these estimates,

together with the gas outflow velocity, an estimate of the source distance and bolometric flux (computed in L93 from the IRAS 12, 25, 60 and $100 \mu\text{m}$ photometry), and the total luminosity; these parameters will be used in Sect. 4 to compare the relation between mid-IR colors and mass loss introduced in paper I, with the new CAMIRAS data.

4. Mid-IR colors and mass loss

The photometric systems of CAMIRAS and TIRCAM (and in general of all mid-IR imaging cameras and photometers) are chosen in order to facilitate the chemical discrimination of astronomical dust.

The O-rich dust present in the AGB circumstellar envelopes having $\text{C/O} \lesssim 1$ is characterized by a mixture of pyroxenes and olivines, collectively known as *astronomical silicates*. The optical properties of silicate dust varies with the associated crystalline or amorphous structure and with the relative amount of Fe and Mg in the silicate stoichiometry, but is in general characterized by two broad features peaked at 9.8 and $18 \mu\text{m}$. These features can easily be detected above or below the continuum emission (according to their occurrence in emission or in absorption) by the 10% passband filters available for CAMIRAS at 9.56 and $16.64 \mu\text{m}$ and for TIRCAM at $9.8 \mu\text{m}$. Several other minor components are assumed to be present in the O-rich dust, among which ice and oxides, to explain the presence of secondary features observed in spectra collected by space, as the $13 \mu\text{m}$ feature seen in a fraction of O-rich IRAS LRS and generally attributed to corundum (Al_2O_3 , see e.g. Onaka et al. 1989; Little-Marenin & Little 1990; Sloan & Price 1995, 1998; but see also Speck 1998, in which SiO_2 is proposed instead). Due to the atmospheric opacity, the wavelengths of these features are not accessible from the ground, and cannot be studied with ground-based mid-IR cameras.

AGB stars having $\text{C/O} \gtrsim 1$ form carbonaceous dust, mostly made of amorphous carbon (“soot”, composed of graphite crystals arranged in amorphous conglomerates), with important secondary components as Polycyclic Aromatic Hydrocarbons (PAH), silicon carbide (SiC) and other carbon bearing condensates. Being the amorphous carbon opacity essentially featureless, the spectral properties of circumstellar envelopes with carbonaceous dust are in general characterized by a narrow emission feature peaked at $11.2 \mu\text{m}$, that can be put in evidence by the

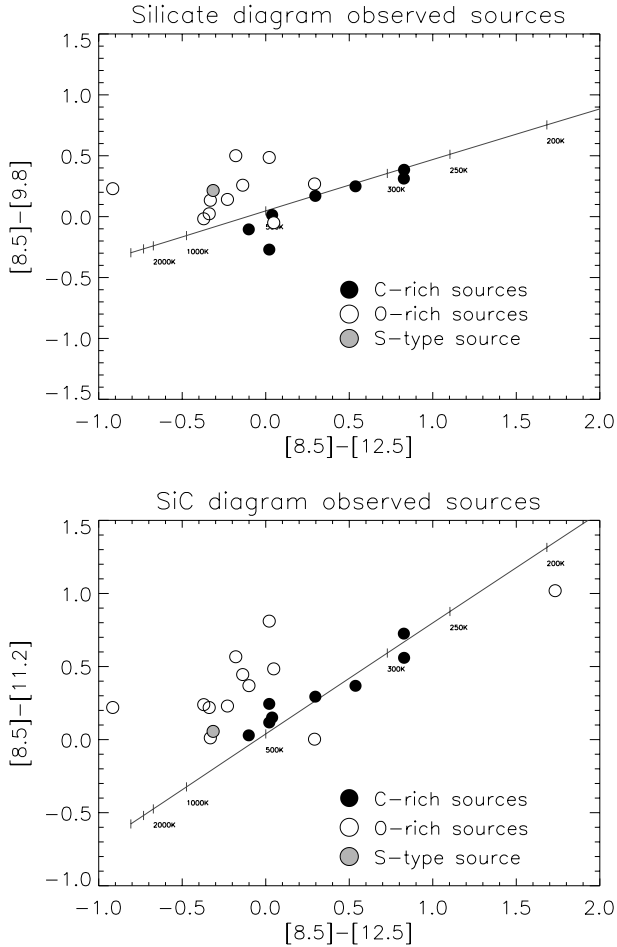


Fig. 1. Color color diagrams of the observed sources (CAMIRAS+TIRCAM). C-rich envelopes are the filled circles, O-rich sources are empty circles and the only S-star is grey. Colors of black bodies with different temperatures are also plotted.

mid-IR filter centered at the same wavelength. PAH emission lines can only be detected in post-AGB and pre-PN objects, having hot central stars whose spectra are rich in the UV radiation needed to populate the transition levels of the PAH molecules; we have attempted PAH detection for a number of sources in Table 1 using the narrow-band filters at 8.57 and 12.24 μm filters, without success (the flux in the PAH filters was similar to the one expected for the continuum).

From the discussion above, it is clear that mid-IR colors based on the 9.8 and 11.2 μm filters might in principle allow one to discriminate sources characterized by silicate and carbonaceous dust; as in paper I we have thus defined the colors $[8.5] - [9.8] = 2.5 \log F_{9.8}/F_{8.55}$ and $[8.5] - [11.2] = 2.5 \log F_{11.21}/F_{8.55}$ as indicators of the strength of the silicate and the SiC features respectively. Both colors use the flux at 8.55 μm (equivalent to the 8.8 μm for TIRCAM sources) as reference for the continuum; a second “continuum” filter at 12.45 μm is used to define the color $[8.5] - [12.5] = 2.5 \log F_{12.45}/F_{8.55}$, which in paper I was proven to measure the “infrared excess” of the sources (e.g. the optical depth of

the envelopes, indication of the amount of dust around the AGB star).

Note that the above color definition ($[1] - [2] = 2.5 \log F_2/F_1$) does not take into account the fluxes of the 0 magnitude star; this choice was made in paper I for consistency with the (IRAS) colors defined in van der Veen & Habing (1988). Equivalent colors calibrated on the zero magnitude fluxes $[1]_0 - [2]_0 = 2.5 \log [(F_2/F_2^0)/(F_1/F_1^0)]$ are related to ours by an offset $\Delta_{[1]-[2]} = ([1]_0 - [2]_0) - ([1] - [2])$, with: $\Delta_{[8.5]-[9.8]} = 0.24$, $\Delta_{[8.5]-[11.2]} = 0.59$ and $\Delta_{[8.5]-[12.5]} = 0.81$.

The “silicate feature” plot in Fig. 1 shows the C-rich sources aligned along a sequence around the black body curve, while the O-rich ones appear to be more dispersed; this different distribution can be explained by considering that the C-rich envelopes are featureless in all the colors of the plot, while the dispersion of the O-rich envelopes is a measure of the strength of the silicate feature. The “SiC feature” plot shows the same pattern, because the silicate feature of the O-rich sources is wide enough to extend into the 11.2 μm filter in the $[8.5] - [11.2]$ color, and the amount of SiC of the C-rich sources in our sample is not high enough to determine a strong dispersion of the sources with carbonaceous dust (at least within the photometric errors). In both plots the more evolved sources have a larger $[8.5] - [12.5]$ color, in agreement with the result found in paper I.

The chosen colors can in principle have a dependance on the phase of the variable sources; we however found that the color variations of sources observed months apart are much smaller than at optical and near-IR wavelengths (see e.g. the source CRL 618 in Table 1 and o Cet in paper I).

To test if the $[8.5] - [12.5]$ color is directly correlated with the amount of dust in the circumstellar envelope (i.e. the mass loss) in paper I the mass loss parameter $2.5 \log [10^5 \dot{M} v_e / L_4]$ was derived from L93 data for all observed sources. C-rich sources were shown to have values of the mass loss parameter linearly related to the $[8.5] - [12.5]$ color. O-rich ones were instead grouped very close to one another, to the point of being undistinguishable within the limits of the photometric and mass loss uncertainty. Two exceptions to this rule were found: a single source in a late evolutionary stage, having a very red color and high mass loss (RAFGL 2205), and an S-star (W And) having intermediate mass loss and a substantial infrared excess. This difference was tentatively explained with the assumptions that: (1) for all sources, a greater IR excess was a measure of higher mass loss; (2) the O-rich sources in the TIRCAM sample, (apart from the more evolved RAFGL 2205), share the same evolutionary stage and thus have similar colors; (3) TIRCAM C-rich sources have a higher mass loss rate but lower IR excesses, because in the 10 μm region the opacity of carbonaceous dust is smaller than that of astronomical silicates.

We have reproduced in Fig. 2 the same mass loss plot already shown in paper I, but including CAMIRAS data. Note how the same regression line of C-stars previously found with TIRCAM holds also for the new C-rich envelopes. The distribution of O-rich stars, instead, now has a much larger spread, both in mass loss and in color. In view of the above interpretation, this would

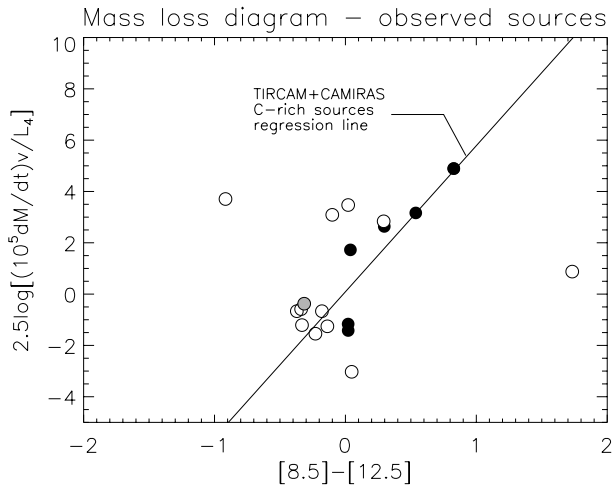


Fig. 2. The mass loss parameter vs. the mid-IR “continuum” color for the observed sources (CAMIRAS+TIRCAM). Again, filled circles are C-rich envelopes, empty ones are O-rich and the S-star is grey. A regression line for C-rich sources is computed and drawn on the diagram. The mass loss parameter is derived from Table 2 (the average value is used for sources with multiple estimates of \dot{M} and L).

be an indication that either the CAMIRAS O-rich sample is less homogeneous than the one observed with TIRCAM, or the previous, weak correlation between mass loss and excess mid-IR color for these sources was simply an effect of low statistics. We have to underline here that some caution is necessary in using the parameters plotted as abscissa (IR color) and ordinate (mass loss) in Fig. 2. Indeed mass loss is derived from radio data on extended regions of the circumstellar envelope, while mid-IR colors probe a more internal dust shell. Different parts of the circumstellar environment may refer to different AGB phases, when the star may have been experiencing different mass loss regimes. Due to this caution, and to the small dimension of the observed sample, we cannot as yet decide which interpretation to favour; for this reason the same analysis will be carried out in the next section using a much larger sample, derived from the L93 catalog, and “simulated” mid-IR colors derived from IRAS LRS.

A final note concerns the color of the S-star W And. As explained in Sect. 3, the $12.5 \mu\text{m}$ flux reported in paper I was found to be contaminated by a residual background signal, and was discarded. The IR color of this star in Fig. 2 is thus computed only using the new CAMIRAS measurements, and places the source in the same region as other O-rich envelopes with low mass loss.

5. Mid-IR color analysis of an extended sample

The catalog collected in L93 contains a list of AGB sources for which millimetric observations of CO and HCN lines are available, giving estimates of the total mass loss rates.

In order to confirm our mid-IR analysis of circumstellar envelopes around mass losing AGB stars with a larger sample, we have selected 154 O-rich, 7 S-type and 167 C-rich sources in

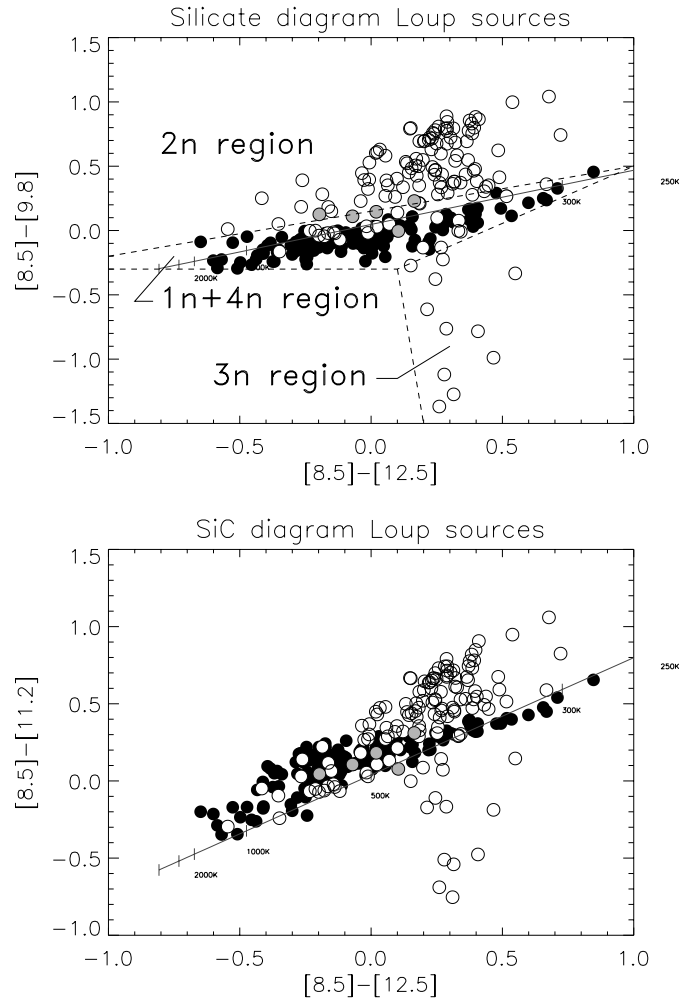


Fig. 3. Color color diagrams of all the selected sources in L93 sample. C-rich envelopes are represented by filled symbols, O-rich ones by empty symbols and S-stars by gray circles. The colors of black bodies with different temperatures are plotted, and the silicate feature diagram is divided in three regions according to the LRS code of the sources.

L93 for which the IRAS LRS is available. Note that the selected sources do not represent a statistically significant sample, since L93 catalog is biased toward strong CO emitters, and the IRAS LRS catalog is affected by source confusion in the Galactic Plane.

For each source the two LRS segments were rectified and spliced together as described in Cohen et al. (1992), and then convolved with CAMIRAS filter profiles to estimate mid-IR photometry and colors in the same photometric system as used in Sect. 4. Fig. 3 shows the silicate and SiC feature color color diagrams obtained with L93 sources of all chemical types: the two plots confirm the distribution of the observed sources, adding pieces of information that are useful for their interpretation, based on the LRS class.

The “silicate feature” diagram in the top panel of Fig. 3, in particular, can be divided into three regions. The first is above the black body curve, and all the O-rich sources of LRS class $2n$ (with the silicate feature in emission) are found here; the

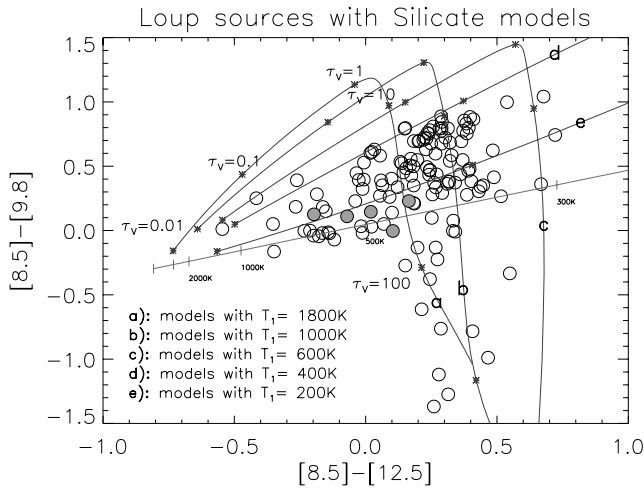


Fig. 4. Color color diagrams of the O-rich and S sources in the L93 sample, plotted with the usual symbols. Model tracks having T_1 of 1800, 1000, 600, 400 and 200 K are plotted; marks on each track indicate models having τ_V of 0.01, 0.1, 1, 10 and 100.

second is aligned along the black body line, and groups all the C-rich sources plus the O-rich ones without the silicate feature (classes $4n$ and $1n$ respectively). Finally, the third region is below the black body line, and collects all the O-rich envelopes of class $3n$ (with the silicate feature in absorption). A similar (but less dispersed) distribution of the O-rich sources is present in the lower panel (“SiC feature” diagram); the C-rich envelopes appear here to have a larger spread *above* the black body, due to the presence of the SiC feature in emission. It is evident that the characteristics of O-rich sources are best recognized in the first plot, while those of C-rich sources are best put into evidence in the second one.

To quantify the distribution of the AGB circumstellar envelopes in the color color diagrams as a function of the envelope physical parameters, we have run a set of simple radiative transfer models of spherically symmetric circumstellar envelopes, using the public domain code DUSTY (Ivezic & Elitzur 1997). Model tracks of envelopes having different optical depths (τ_V from 0.01 to 100) are computed assuming steady mass loss (radial density $\rho \sim r^{-2}$) and dust opacities from Ossenkopf et al. (1992) for silicates, from Hanner (1988) for amorphous carbon and from Pégourié (1988) for SiC. The central AGB star spectral energy distribution is simulated by a black body at the temperature of 2500 K.

Fig. 4 shows model tracks computed with silicate dust opacity superimposed on the O-rich sources. Each curve corresponds to a different temperature T_1 of the inner envelope boundary R_1 , where R_1 is either the dust condensation radius (if the dust is presently being produced), or the radius of the internal cavity generated by the envelope expansion (if the mass loss is presently quiescent). Note that the whole area occupied by the color distributions of the observed sources is also covered by model tracks with different model parameters, and a wide range of temperatures T_1 is necessary to explain mid-IR colors of all sources, in particular those having weak silicate features

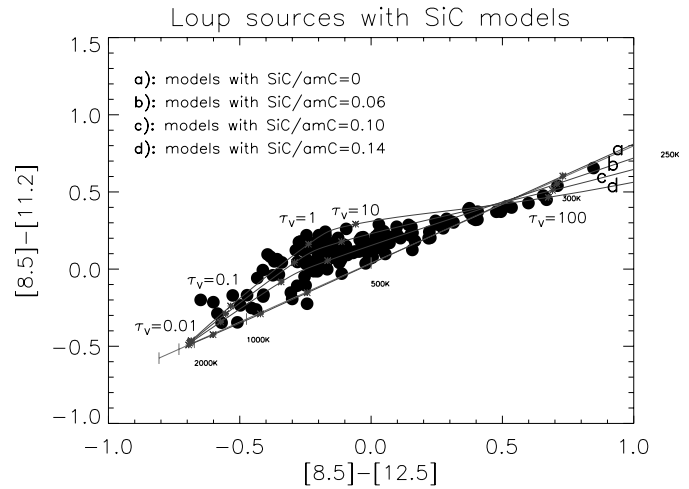


Fig. 5. Color color diagrams of the C-rich sources in the L93 sample. Model tracks having SiC/amC of 0, 0.06, 0.10 and 0.14 are plotted; marks on each track indicate models having τ_V of 0.01, 0.1, 1, 10 and 100.

and small infrared excesses, that require cold envelopes to be modelled. We will discuss in greater detail the modelling of O-rich envelopes in a separate paper, focussing on the correlations between the temperature T_1 and the variability type (Mira, semiregular or irregular) of an even larger sample. Note, finally, that model tracks for different T_1 join in the region of maximum source density. This means that the same silicate feature strength, relative to the continuum, can be obtained either with high T_1 and $\tau_V \gtrsim 1$ or with low T_1 and $\tau_V \lesssim 1$, and the two cases cannot be well separated on the basis of the mid-IR colors alone. To derive in a unique way the physical parameters of O-rich AGB circumstellar envelopes thus requires either to consider the whole LRS distribution, or to fit, together with the mid-IR colors, also the photometry at 12 and 25 μm (plus the fluxes at 60 and 100 μm whenever they are not affected by “cirrus” contamination).

A similar plot is shown in Fig. 5 for all C-rich sources and models computed with amorphous carbon opacity mixed with different amounts (from 0 to 0.14) of SiC. The position of the model tracks confirms that the color distribution of the sources depends on the abundance ratio of SiC to amorphous carbon, and that the relative proportion of the two dust components can be estimated (at least for moderate τ_V) by a fitting to the mid-IR colors. Note that for the L93 sample the maximum amount of SiC in the dust mixture is of the order of 14%, (in number density of the dust grains) confirming that it is not a major component of C-rich dust.

Since for all L93 sources at least one mass loss estimate is available, we have reproduced in Fig. 6 the mass loss parameter vs. mid-IR color for the whole sample. The sources of different chemical type are not completely separated in the plot, but the C-rich sources appear to be more concentrated in the upper left side of the diagram (higher mass loss, lower infrared excess), while the O-rich ones are grouped in the lower right side (higher

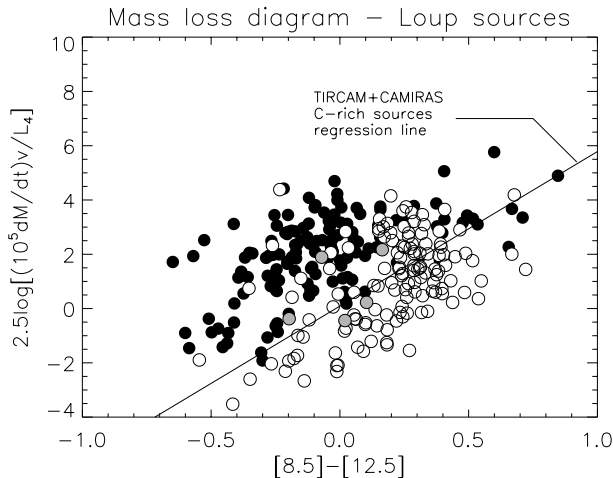


Fig. 6. The mass loss parameter vs. mid-IR color for all sources in L93. As usual, the symbols (circles) for C-rich sources are filled, for O-rich sources are empty and for S-stars are grey. The regression line computed for the ground-based observations (TIRCAM+CAMIRAS) is reproduced in the diagram.

infrared excesses and lower mass loss rate), with the few S-stars in between.

The regression line previously found through ground based mid-IR observations of C-rich AGB stars defines a sort of lower boundary of the region populated by C-rich envelopes in the L93 sample. This is probably a consequence of the selection process in which the targets to be observed were chosen. In order to maximize the S/N ratio achievable with TIRCAM and CAMIRAS detectors, we have selected the brightest sources with the largest infrared excess available: in the case of the C-rich envelopes this favoured the sources at the lower boundary of the color distribution, that is where the infrared excess is maximum.

In general, the L93 sources confirm the interpretation given in paper I and reported in Sect. 4, according to which C-stars tend to have lower infrared excesses for a given mass loss rate as compared to O-rich sources, due to the intrinsic optical properties of the dust particles in the two cases.

Even though the error bars on the estimates of mass loss rate in the L93 sample are quite large (in general larger than the error for the better defined TIRCAM and CAMIRAS samples), it is unlikely that the errors on \dot{M} alone can explain the spread in the source distribution shown in Fig. 6. This favours the idea that the spread is intrinsic to the sample, and possibly due to temporal variations in the mass loss rates on timescales smaller than the crossing time of the circumstellar envelope at the stellar wind speed. Since the L93 mass loss estimates are based on CO emission taking place in a shell of radius r_{CO} of the order of 10^{17} cm, while the mid-IR photosphere is usually at a distance of about 10^{14} – 10^{15} cm, in order to break the correlation between the gaseous and the dusty envelopes we need to postulate temporal variations of \dot{M} on timescales of the order of 10^3 yr (assuming an outflow velocity of 10 km s $^{-1}$), or shorter. This timescale is in general too short to be associated with the

thermal pulses of the AGB phase, and too long with respect to the LPV variability, but is compatible with the temporal separation of the structures observed in the remnant AGB shells of post-AGB objects like the Egg Nebula (Sahai et al. 1998), perhaps associated with dynamical times of dust condensation or with low frequency variability created by interference of close-by dynamical modes (but see also Mastrodemos & Morris 1998 for an alternative hypothesis involving the “evaporation” of a close companion due to the AGB wind).

6. Images of extended sources

Radiative transfer modelling allows one to determine the main physical and chemical parameters of dusty circumstellar envelopes by a model fitting of their mid-IR spectral energy distribution (7 – 23 μ m, as in the IRAS LRS); this however requires underlying assumptions about the geometry of the system. Since the source spectra alone do not provide sufficient information to fit the extra free parameters introduced by a complex geometry, spherical symmetry and steady mass loss (density $\rho \sim r^{-2}$) have usually to be assumed. This is an important limitation, since observational evidences at several wavelengths indicate deviations from spherical symmetry in AGB and post-AGB objects (Hora et al. 1996; Dayal et al. 1998; Skinner et al. 1998; Bujarrabal et al. 1992; Dyck et al. 1987; Barnbaum et al. 1995; Kastner & Weintraub 1994). Also a non homogeneous radial density distribution often appears characterized by detached shells (Hashimoto et al. 1998; Olofsson et al. 1992; Willems & de Jong 1988; Zijlstra et al. 1992) and clumpy structures (Lopez et al. 1997; Olofsson et al. 1996; Weigelt et al. 1998) that can be related to different phenomena (temporal modulation of the mass loss rate and of the dust condensation mechanisms; presence of a close companion; building of a circumstellar disk, etc...).

It is thus evident that the availability of spatially resolved images of AGB circumstellar envelopes, coupled with two- or even three-dimensional radiative transfer codes (see e.g. Lopez et al. 1995) would greatly improve our knowledge of the mass loss processes in the latest stages of the AGB evolution. The development of infrared interferometry (see e.g. Monnier et al. 1997 and previous work) and the extension of interferometric techniques to mid-IR wavelengths (Sudol et al. 1999) have recently made possible to obtain one-dimensional visibility curves of AGB envelopes that were previously unresolved at 10 μ m. The direct two dimensional imaging of these sources, however, is still limited in the mid-IR by diffraction, because of the small size of the envelope regions emitting in the mid-IR (10 – 100 A.U.) that restricts the possibility of obtaining spatially resolved maps at 10 μ m to the brightest and nearest objects.

Due to the small aperture of the TIRGO telescope (1.5 m), most of the observed sources appear to be spatially unresolved in our observations. There are, however, some exceptions in which the images show departures from spherical symmetry and extended emissions beyond the instrumental Point Spread Function (PSF). We will discuss them in a separate paper but, as an example, we present in Fig. 7 the image of the best resolved

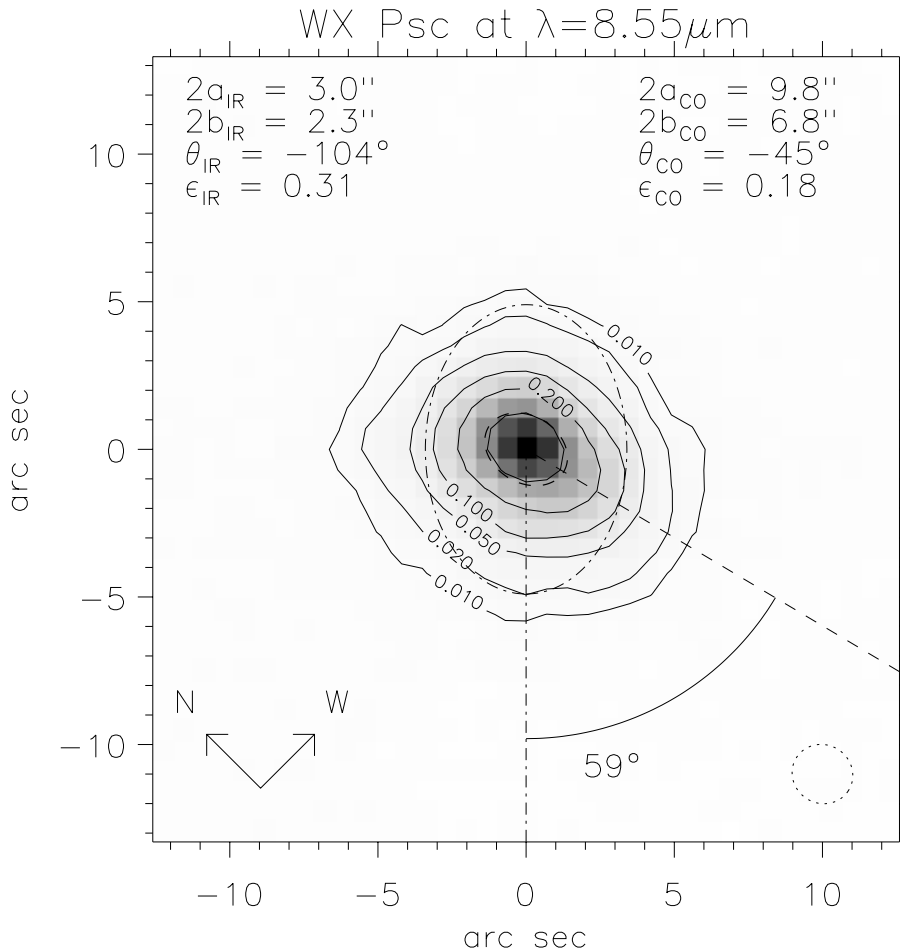


Fig. 7. Images and contour plots of the O-rich AGB envelope WX Psc at $8.55\mu\text{m}$. Contour levels are shown at 0.01, 0.02, 0.05, 0.1, 0.2 and 0.5 of the source maximum, where the 0.01 contour corresponds to the 5σ noise level. The source radial brightness distribution is fitted with a 2D elliptical gaussian whose major and minor axis, orientation (from East direction, clockwise) and asymmetry are indicated in the left column. The “sizes” a and b of the interpolating elliptical gaussian are related to the FWHM by the relation $\text{FWHM} = \text{size} \cdot \sqrt{2 \ln 2}$. The dashed contour and line are the half maximum ellipse of the fitting gaussian, and the orientation of its major axis. The dot dashed contour and line indicate the size and orientation of the secondary gaussian component of the CO ($J=1\rightarrow 0$) emission as measured by Neri et al. (1998). The parameters of the CO fitting are indicated in the right column for comparison; note the 59° rotation between the orientation of the IR and the CO major axis. The dotted circle in the lower right corner is the beam size of the PSF, derived from the half maximum contour of a standard star.

source showing a non-spherical geometry, i.e. the bright O-rich AGB star WX Psc (alias CIT 3) at $8.8\mu\text{m}$.

This source has been recently observed at $11.5\mu\text{m}$ at the Wyoming Infrared Observatory (see Sudol et al. 1999), where the visibility curve in the E-W direction was derived, and no extension was found (leading to the conclusion that at that wavelength the circumstellar shell should have an angular diameter of $0.63''$ or less). Similarly, a far-IR search (60 and $100\mu\text{m}$) in the IRAS database conducted by Young et al. (1993) was not able to resolve extended emission from the source.

Near-IR speckle observations at the SAO 6m telescope (Irgang et al. 1998), however, were able to identify two separate components in the circumstellar envelope of the source, consisting of a partially resolved smaller structure (representing the innermost region of the envelope) and a fully resolved extended nebulosity that “[...] might point to a change of the physical properties in the outflow”.

High resolution ^{12}CO ($J=1\rightarrow 0$) and ($J=2\rightarrow 1$) maps of the O-rich source have been obtained using radio interferometers and could resolve the molecular envelope of this object. In Neri et al. (1998) IRAM observations of WX Psc are fitted using a double component envelope in which the primary component (of size $\sim 30''$) is spherical and the secondary one is elliptical, with asymmetry $\epsilon_{\text{CO}} = 0.18$ (major and minor sizes $9.8''$ and $6.8''$) and major axis rotated by 45° from E to S.

We have attempted a similar 2D gaussian fit on our $8.55\mu\text{m}$ image (not deconvolved with the PSF), and the results are shown in Fig. 7. The best fit parameters indicate an elongated shape (major and minor size of $3.0''$ and $2.3''$ respectively) with asymmetry $\epsilon_{\text{IR}} = 0.31$, oriented with the major axis at 104° from the E direction (counterclockwise). The comparison of the source image with the PSF derived from nearby standard stars (symmetrical and with FWHM of about $2.0''$), implies an extension of WX Psc in the N-S direction, while the source remains unresolved along the E-W axis (in agreement with Sudol et al. 1999 observation). The extension of the source is less clear in our images at longer wavelengths, due to the larger size of the (diffraction limited) PSF in those cases.

The smaller dimensions of the mid-IR image, compared to the CO map, its larger asymmetry and the different orientation (59° rotation between the CO and the IR envelope) suggest the possibility that the mid-IR and the CO observations refer to physically distinct regions of the envelope. This consideration, together with the failure to detect an extended dust emission at 60 and $100\mu\text{m}$, leads to the conclusion that in the envelope of WX Psc the dust appears to be concentrated only in the central regions, close to the stellar photosphere, where it presumably condensed in a non spherical environment. At larger distances from the central star the dust is undetectable. The progressive decrease in the envelope asymmetry probed by the CO obser-

vations can be explained either assuming a disk-like geometry in the dust spatial distribution, or, alternatively, assuming an axisymmetrical circumstellar envelope that becomes more and more spherical as it expands due to the AGB wind.

Even though the spatial resolution of our observation does not allow us to decide between these two concurrent hypotheses, it puts in evidence that also the AGB phase (and not only the later stages of post-AGB and pre-PN) can be characterized by strong deviations from spherical symmetry. They shape the dust component of the circumstellar envelope, and are detectable using mid-IR imaging. It is clear, however, that only a limited number of AGB envelopes can be spatially resolved in the mid-IR using a 1.5m telescope: our test only shows that even with such a small aperture it is possible to derive information on the spatial distribution of dust for some bright and close-by sources. A detailed discussion of the other images obtained with CAMIRAS at TIRGO, and of simulations aimed at compiling a list of sources that can be resolved with larger aperture infrared telescopes (IRTF, UKIRT and the future LBT interferometer) will be presented in a forthcoming paper.

7. Conclusions

The advent of semiconductor array detectors sensitive in the mid-IR range have made possible in the last decade the full development of infrared astronomy in the 5-20 μm window. The IRAS and ISO missions, with their collections of medium and high resolution spectra, have changed our understanding of the molecular and dusty circumstellar environment, giving a contribution at least comparable to the one given by spectral observations in the visible, near-IR or radio. The same is not true for mid-IR imaging, that is still limited by low sensitivity due to imperfect background subtraction, narrow fields of view, etc.

The upcoming availability of large format arrays with shorter readout time (allowing a better correction of atmospheric seeing and background emissions), and the recent advent of large aperture telescopes for mid-IR astronomy, are soon going to change this situation, and will probably allow the acquisition of large field – high spatial resolution – images, with increasing sensitivity, even from the ground. For this reason we have analyzed, in this paper, the current state of mid-IR ground based imaging of circumstellar AGB envelopes, using a set of observations made with two different imaging cameras; we have also modelled data derived from the IRAS database, to develop diagnostic tools for the physical and chemical status of dust in the AGB systems.

The comparison of our data with the simulations, showed that by choosing a suitable photometric system (using filters centered at the wavelengths of silicate and SiC features, and at the dust continuum emission) it is possible to put in evidence a different distribution of C-rich and O-rich sources in the color-color diagrams introduced in Sect. 4. We found the same pattern for data taken with different imaging cameras (having similar but not coincident photometric systems) and for the simulated photometry: (1) an alignment of the C-rich objects along the black body curve and (2) a much larger dispersion of O-rich en-

velopes according to the strength of their silicate features. Even though the separation between the two species is not unique, we have verified that mid-IR photometry, coupled with the IRAS photometric data (available for most of galactic AGBs) is sufficient to specify the physical and chemical status of dust in the circumstellar environment.

A loose correlation found in Sect. 5 between [8.5]-[12.5] color and a mass loss parameter derived by radio observations, reflects a general tendency of having larger infrared excesses for higher mass loss rates, but also the differences in the optical properties of silicate and carbonaceous grains. A residual scatter present in the source distribution on the diagram, was tentatively explained as an indication of possible temporal variations in the dust production, on a temporal scale of 10^3 yr, or less.

We believe that our analysis confirms the value of mid-IR multicolor photometry in investigating the properties of AGB circumstellar envelopes; even though the quality of the informations that our color-color diagrams provide cannot match the details given by medium or high resolution spectra, the possibility to study a much larger sample of fainter sources still makes the photometric technique the most suitable for a statistical analysis of large samples.

The main potentialities of mid-IR cameras lie in their imaging capabilities; as shown by the image of the source WX Psc in Sect. 6, the possibility to resolve the spatial structure of AGB envelopes can provide valuable insights on mass loss history and the symmetry of specific sources. The availability of instruments providing better angular resolution and higher sensitivity will permit to spatially resolve a larger number of targets, thus making mid-IR imaging a very important tool for the investigation of dust condensation in circumstellar environments and for understanding mass loss processes during the AGB phase.

Acknowledgements. This research made use of the LRS database maintained at the University of Calgary and the SIMBAD database at Strasbourg. We acknowledge funding from the Italian MURST *Progetto di Cofinanziamento "Evoluzione Stellare"*. The data analysis of this work was partially funded by the Consorzio Nazionale per l'Astronomia e l'Astrofisica under contract 16/97. We are indebted to the staff of the TIRGO telescope and to that of the CAMIRAS project for assistance during the observations.

References

- Barnbaum C., Morris. M., Kahane C., 1995, ApJ 450, 862
- Blöcker T., Schönberner D., 1991, A&A 244, 43
- Blommaert J.A.D.L., van der Veen W.E.C.J., van Langevelde H.J., Habing H.J., Sjouwerman L.O., 1998, A&A 329, 991
- Bujarrabal V., Alcolea J., Planesas P., 1992, A&A 257, 701
- Busso M., Origlia L., Marengo M., et al., 1996, A&A 311, 253 (paper I)
- Busso M., Gallino R., Wasserburg G.J., 1999, ARA&A, in press
- Cohen M., Walker R.G., Witteborn F.C., 1992, AJ 104, 2030
- Dayal A., Hoffmann W.F., Biegging J.H., et al., 1998, ApJ 492, 603
- Dyck H.M., Zuckerman B., Howell R.R., Beckwith S., 1987, PASP 99, 99
- Engelke C.W., 1992, AJ 104, 1248
- Frost C.A., Cannon R.C., Lattanzio J.C., Wood P.R., Forestini M., 1998, A&A 332, 17

- Fleischer A.J., Gauger A., Sedlmayr E., 1992, *A&A* 266, 321
Gezari D.Y., 1993, *Atlas of Infrared Observations*. NASA
Hanner M.S., 1988, *NASA Conf. Pub.* 3004, 22
Hashimoto O., Izumiura H., Kester D.J.M., Bontekoe T.J.R., 1998, *A&A* 329, 213
Hora J.L., Deutsch L.K., Hofmann W.F., Fazio G.G., 1996, *AJ* 112, 2064
Iben I. Jr., Renzini A., 1983, *ARA&A* 21, 271
IRAS Catalogues and Atlases, *Atlas of Low Resolution Spectra*, IRAS Science Team, 1986, *A&AS* 65, 607
Irrgang P., Balega Y.Y., Gauger A., et al., 1998, poster P4-08 presented at the I.A.U. Symposium no. 191 on Asymptotic Giant Branch Stars. Montpellier, France, Aug 28-Sept 1, 1998
Ivezic Ž., Elitzur M., 1997, *MNRAS* 287, 799
Kastner J.H., Weintraub D.A., 1994, *ApJ* 434, 719
Lagage P.O., Jouan R., Masse P., Mestreau P., Tarrus A., 1992, In: Ulrich M.H. (ed.) 42nd ESO Conf., *Progress in Telescope and Instrumentation Technologies*. ESO, Munich, p. 601
Le Bertre T., Winters J.M., 1998, *A&A* 334, 173
Little-Marenin I.R., Little S.J., 1990, *AJ* 99, 1173
Lopez B., Mékarnia D., Lefèvre J., 1995, *A&A* 296, 752
Lopez B., Danchi W.C., Bester M., et al., 1997, *ApJ* 488, 807
Loup C., Forveille T., Omont A., Paul J.F., 1993, *A&AS* 99, 291 (L93)
Marengo M., Canil G., Silvestro G., et al., 1997, *A&A* 322, 924 (paper II)
Mastrodemos N., Morris M., 1998, *ApJ* 497, 303
Monnier J.D., Bester M., Danchi W.C., et al., 1997, *ApJ* 481, 420
Monnier J.D., Geballe T.R., Danchi W.C., 1998, *ApJ* 502, 833
Neri R., Kahane C., Lucas R., Bujarrabal V., Loup C., 1998, *A&AS* 130, 1
Olofsson H., Carlström U., Eriksson K., Gustafsson B., 1992, *A&A* 253, L17
Olofsson H., Bergman P., Eriksson K., Gustafsson B., 1996, *A&A* 311, 587
Onaka T., de Jong T., Willems F.J., 1989, *A&A* 218, 169
Ossenkopf V., Henning Th., Mathis J.S., 1992, *A&A* 261, 567
Pégourié B., 1988, *A&A* 194, 335
Renzini A., Voli M., 1981, *A&A* 94, 175
Sackmann I.-J., Boothroyd A.I., 1992, *ApJ* 392, 71
Sahai R., Trauger J.T., Watson A.M., et al., 1998, *ApJ* 493, 301
Skinner C.J., Meixner M., Bobrowsky M., 1998, *MNRAS* 300, L29
Sloan G.C., Price S.D., 1995, *ApJ* 451, 758
Sloan G.C., Price D., 1998, *ApJS* 119, 141
Smith V.V., Lambert D.L., 1989, *ApJ* 345, L75
Speck A.K., 1998, Ph.D. Thesis, University College London, University College London Gower Street, London WC1N 1AS
Steffen M., Szczerba R., Schönberner D., 1998, *A&A* 337, 149
Straniero O., Gallino R., Busso M., et al., 1995, *ApJ* 440, 85
Staniero O., Chieffi A., Limongi M., et al., 1997, *ApJ* 478, 332
Sudol J.J., Dyck H.M., Stencel R.E., Klebe D.I., Creech-Eakman M.J., 1999, *AJ* 117, 1609
Sugimoto D., 1971, *Progr. Theor. Phys.* 45, 761
van der Veen W.E.C.J., Habing H.J., 1988, *A&A* 194, 125
Vassiliadis E., Wood P.R., 1993, *ApJ* 413, 641
Wallerstein G., Knapp G.R., 1998, *ARA&A* 36, 369
Waters L.B.F., Beintema D.A., Zijlstra A.A., et al., 1998, *A&A* 331, L61
Weigelt, G., Balega Y., Blocker T., et al., 1998, *A&A* 333, L51
Willems F.J., De Jong T., 1988, *A&A* 196, 173
Winters J.M., Fleischer A.J., Gauger A., Sedlmayr E., 1994, *A&A* 290, 623
Winters J.M., Fleischer A.J., Gauger A., Sedlmayr E., 1995, *A&A* 302, 483
Young K., Phillips T.G., Knapp G.R., 1993, *APJS* 86, 517
Zijlstra A.A., Loup C., Waters L.B.F.M., de Jong T., 1992, *A&A* 265, L5
Zijlstra A.A., Loup C., Waters L.B.F.M., et al., 1996, *MNRAS* 279, 32